Quasi-static displacement calibration system for a 'Violin-Mode' shadow-sensor in Advanced LIGO suspensions

N.A. Lockerbie and K.V. Tokmakov

SUPA (Scottish Universities Physics Department) Department of Physics, University of Strathclyde, 107 Rottenrow, Glasgow G4 0NG, UK.

Abstract. This paper describes the design of, and results from, a calibration system for optical linear displacement- (shadow-) sensors. The shadow-sensors were designed to detect 'Violin-Mode' (*VM*) resonances in the 0.4 mm diameter silica fibre suspensions of the test-masses / mirrors of advanced LIGO gravitational wave interferometers. Each sensor illuminated the fibre under test, so as to cast its narrow shadow onto a 'synthesized split photodiode' detector, the shadow falling over adjacent edges of the paired photodiodes. The apparatus described here translated a vertically orientated silica test fibre horizontally through a collimated Near InfraRed illuminating beam, whilst simultaneously capturing the separate *DC* 'shadow notch' outputs from each of the paired split photodiode detectors. As the ratio of *AC* to *DC* photocurrent sensitivities to displacement was known, a calibration of the *DC* response to quasi-static shadow displacement allowed the required *AC* sensitivity to vibrational displacement to be found. Special techniques are described for generating the required constant scan-rate for the test-fibre using a *DC* motor-driven stage, for removing 'jitter' at such low translation rates from a linear magnetic encoder, and so for capturing the two shadow-notch signals at each micrometre of the test-fibre's travel. Calibration, across the four detectors of this work, gave a vibrational responsivity in voltage terms of (9.45 ± 1.20) MV (rms) / metre (rms), yielding a *VM* displacement sensitivity of (69 ± 13) picometres (rms) / $\sqrt{\text{Hz}}$, at 500 Hz, over the required measuring span of ± 0.1 mm.

1. Introduction

1.1. Background

A prototype system of four shadow-sensors was designed to be retro-fitted to an advanced LIGO (Laser Interferometer Gravitational wave Observatory) test-mass / mirror suspension, in which a 40 kg test-mass was suspended by four fused silica fibres. The dimensions of the fibres were approximately 600 mm long by 0.4 mm in diameter [1–5]. These shadow-sensors—one per fibre—each comprised an emitter and a detector, which bracketed the illuminated fibre. The emitter was in the form of a collimated source of Near InfraRed (NIR) illumination, coming from a column of miniature LEDs [9], such that the source cast a vertical shadow of its illuminated fibre onto the facing detector. The corresponding detector was a 'synthesized split-photodiode,' and this was optimized for its (differential) response to lateral shadow displacement [8]. A schematic cut-away diagram of the shadow-sensor is show in Figure 1, and a photo of it is presented in Figure 2—the shadow-sensor as a whole being described in detail in [8,9].

The primary purpose of the full detection system was to monitor any transverse 'Violin-Mode' (*VM*) resonances that might be excited on these fibres [10], since the frequencies of these fundamental modes and their harmonics spanned the gravitational wave detection bandwidth. However, the system of shadow-sensors was capable also of detecting any 'large amplitude,' very low frequency, transverse pendulum-mode motion of the test-mass and its suspension fibres (at ~ 0.6 Hz) [10,11]. Once detected, the oscillatory motion of the suspension fibres then could be cold-damped, actively [6,7]. *VM* resonances in the highly-tensioned silica suspension fibres were found to have fundamental frequencies ~ 500 Hz, and for this application the shadow-sensors were required to have a fibre- (i.e., a

1

shadow-) displacement sensitivity of 100 picometres (rms) / √Hz over a ±0.1 mm range of fibre position, at this frequency.

1.2. *The displacement calibration procedure*

The displacement calibration system for the shadow-sensors, which is described here, was designed and built in order to help confirm that the displacement sensitivity of the full detection system met the target value given above. Naturally, this confirmation fell into two parts: firstly, a determination of the raw displacement responsivity, in volts per metre of fibre displacement; and secondly, a determination of the intrinsic noise level at the detection amplifier's output, this being in the form of noise Power Spectral Density, measured in volts^2 / Hz, or (more usefully) in the form of noise Amplitude Spectral Density, measured in volts (rms) / √Hz—at (say) 500 Hz. The work reported here addresses the first part, i.e., the calibration of the displacement responsivity. The noise performance of the shadow-sensors has been described elsewhere [8,9].

In order to measure their displacement responsivities, each of the four emitter-detector pairs underwent the following calibration procedure, with the relative emitter / fibre / detector distances mimicking those of a *VM* sensor installed in an actual test-mass suspension: a vertically-orientated silica fibre test sample (diameter = 0.4 mm) was moved horizontally, at a steady translation rate, so as to pass from side-to-side through the emitter under test's static, collimated, NIR beam (λ = 890 nm), as shown in Figure 1. In this way, the fibre cast a moving shadow onto the facing, fixed, detector. Simultaneously, the *DC* (photocurrent-derived) voltages from the two sensing elements in each detector were recorded as a function of fibre (i.e., of shadow) position—at every 1 μm incremental change in its position, in fact. The Emitter-to-fibre and Detector-to-fibre stand-off separations were each 20 mm.

1.3. *'Shadow notch' measurements*

The shadow-sensor's detector comprised two adjacent rectangular ('tall, narrow': 29.1 mm × 0.86 mm) photodiode elements, with essentially no dead-band between them. Thus, as the fibre's shadow passed over each of these elements, in turn, it caused a 'shadow notch' to appear in their respective *DC* response—as shown in Figure 11. By differentiating these signals off-line with respect to test-fibre position (ξ), the rate of change of differential *DC* voltage with fibre position—i.e., the *DC* displacement responsivity—was found. However, the dimensionless ratio of *AC* to *DC* photocurrent (shadow-displacement) responsivity was determined in advance by the design of the transimpedance amplifier used. Nominally, this ratio had a value of 1000, mid-band [13]. Therefore, a calibration of the '*DC* responsivity to quasi-static displacement' allowed the required '*AC* responsivity to vibrational displacement' to be deduced, at any vibrational frequency (500 Hz, say).

Therefore, a 'bespoke' piece of apparatus was designed and constructed so that these *DC* displacement responsivity measurements could be made. A test-fibre holder was constructed, shown both schematically and in the photo of Figure 2, and this was attached to the carriage of a low-cost manual leadscrew-actuator stage, with a 190 mm stroke. The stage itself then was adapted to be driven at a regulated, constant, speed by a *DC* motor coupled to an in-line planetary gearbox. The position of the fibre was recorded with a resolution of ±1 μm by retro-fitting an inexpensive commercial linear magnetic encoder to the stage. However, it turned out that the encoder needed to be adapted for this work, and this was accomplished by fitting it with a digital interface. This interface eliminated the natural jitter encountered in the encoder's quadrature phase outputs at the very low

translation rates which were used: ~ 0.2 mm s^{-1} at maximum, down to below 1 μm s^{-1}. Both the constant speed drive for the *DC* motor, and the digital interface for the encoder, are described in §5.

Although the shadow-sensor calibration system was designed and built in order to accomplish a specific task, the novel scientific and technical solutions chosen, as well as the modular design, naturally would lend themselves to other high precision optical scanning applications.

2. The shadow-sensor

A cut-away schematic view of the shadow-sensor used in this work is shown in Figure 1. The source of illumination in the Emitter was a single column of 16 × OP224 NIR LEDs, arranged as two strings of 8 series-connected LEDs (for redundancy), with alternate LEDs belonging to the same string [9]. Only one string was active at any time, this being powered by a constant current of 25 mA. The radiation (λ = 890 nm) from this source was collimated by the 80 mm Focal Length lens, and this cast a moving shadow of the illuminated fused silica fibre sample onto the Detector—the shadow moving at the same speed as the fibre. The detector was a synthesized split-photodiode, outlined in §1.3, above [8]. The *DC* output voltages derived from the detector's two sensing elements, denoted here by V*DC*,a and V*DC*,b, were captured at every 1 μm increment of fibre position, with 12-bit accuracy, typically over a measuring span of 15 mm.
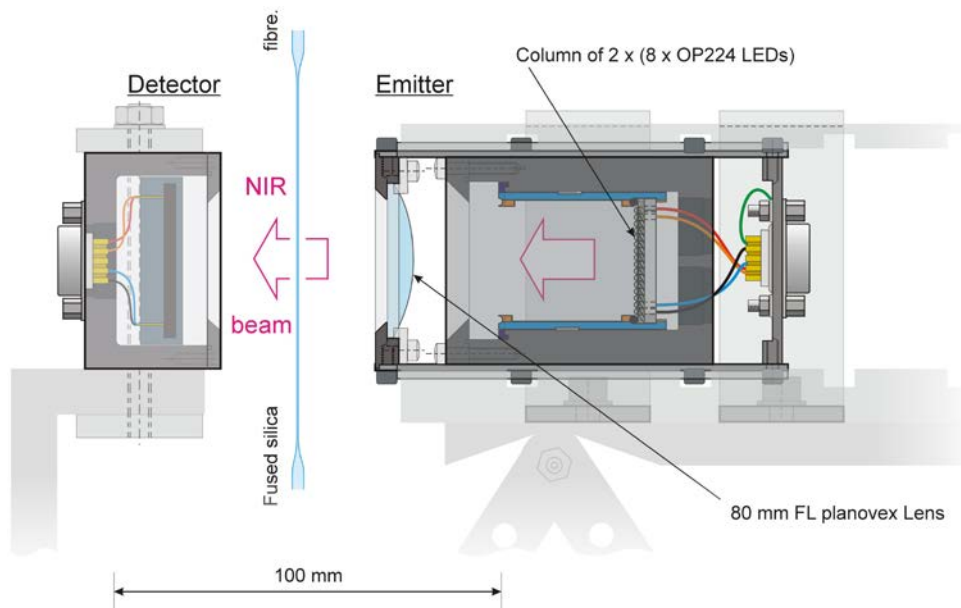

Figure 1. Schematic cut-away view of the shadow-sensor (Emitter + Detector), which was mounted rigidly onto an optical plate, as shown in Figures 2 and 4. The test-fibre sample was moved at a constant rate of traverse so as to cut through the sensor's NIR beam at right angles to its optic-axis (i.e., in this Figure either into, or out of, the page). Please refer to the text.

3. The test-fibre holder

The holder, which was used to keep the silica test-fibre sample under tension, is shown in Figure 2. It was bolted to the carriage of an *Ondrives* LA7-30002 leadscrew-actuator stage, the stage itself being driven by a *DC* motor via a 1621:1 planetary reduction gearbox (motor: 9 volt *Maxon A*-max 110119, and gearbox: *Maxon* GP 22 A 110341). The fibre

was attached at its upper end to a pivoted tensioning arm, which was provided with a knurled tension adjustment knob, whilst the lower end of the fibre was attached to the free end of load-cell having a 10 kg wt. Full Scale (the test-fibre was much shorter than the 600 mm used in aLIGO, and so a smaller tension was adequate for this calibration work—as indicated in the Figure caption). This load cell, together with its signal-conditioning interface, allowed the actual tension in the fibre to be monitored, and adjusted.
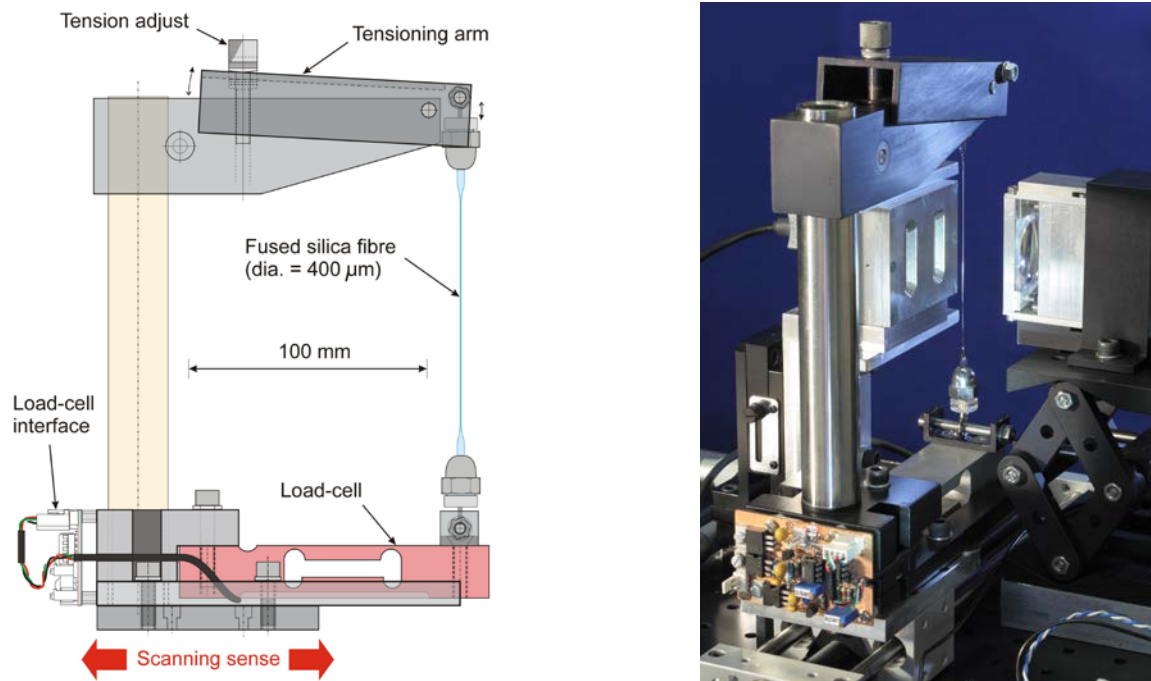
Figure 2. Left: silica test-fibre holder, showing the tensioning arrangement, and tension monitoring system. In the work reported here, the tension was set to 0.55 kg.wt. The holder was bolted onto the carriage of a linear translation stage. Right: photo of the silica test-fibre as it was being scanned transversely through the shadow-sensor's NIR beam. A dual shadow detector housing is shown at the rear, centre left, of the photo. Here, only the rightmost of the two synthesized-split-photodiode detectors (viewed from the front of the housing) was being employed. The NIR emitter is on the right of the photo.

4. The triple-output transimpedance amplifier

The transimpedance amplifier used in this work is shown schematically in Figure 3. It is described in detail elsewhere [13]. The left side of Figure 3 shows in plan view an incident, collimated, NIR beam illuminating a suspension fibre—here illuminating it from the left. The continuation of this incident beam, together with the shadow cast by the fibre, next falls across the facing ridge of a 45°–90°–45° Au/Cr mirror-coated beam-splitting prism. The reflected (split) NIR beam then is incident, albeit differentially, onto the two photodiode detector elements labelled PDa and PDb, generating within these elements the photocurrents i_{PDa} and i_{PDb}, respectively, as indicated in the Figure.

In Figure 3, these two photocurrents form the signal inputs to the 'Transimpedance Amplifiers' block, which functioned as follows: the mean, 'DC,' components of these photocurrents were amplified to yield the (positive) DC output voltages VDC,a and VDC,b, mentioned above in §2, where both of these voltages were generated through a transimpedance gain of R = 120 kΩ. Any AC photocurrent components, however, were amplified along separate transduction pathways, so that for these components the transimpedance gains were 10× higher (at R = 1.2 MΩ), yielding the intermediate AC voltages VAC, a and VAC, b in Figure 3—these voltages being in natural anti-phase.

4

These two *AC* voltages were differenced—thereby doubling the signal's size—before being amplified further by a factor of 100, as indicated in the Figure, to yield the single Violin-Mode *AC* output voltage, *VM AC*. In practice, the *AC* pass-band of this amplifier extended from 226 Hz–8.93 kHz (–3 dB points).

Therefore, the nominal *AC* to *DC* differential (shadow-) displacement responsivities stood in the ratio 1000:1 (mid-band). In practice, due to the amplifier's circumscribed pass-band, and roll-off towards both high and low frequencies, this dimensionless ratio was found to be 976 ±4 mid-band, at 1.48 kHz, and 904 ±4, at 500 Hz.
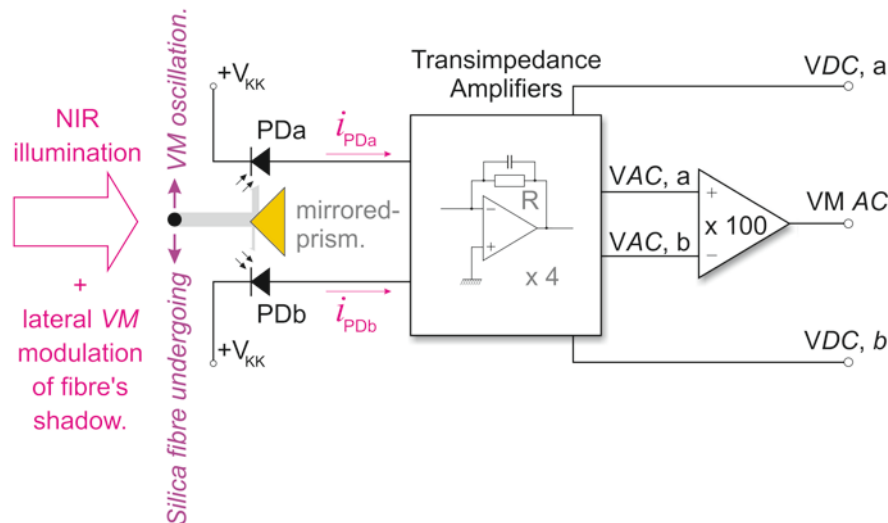
Figure 3. 'Plan view' schematic of the *VM* shadow-detector and its Transimpedance Amplifiers for an individual silica test-fibre. The collimated Near InfraRed beam illuminating the suspension fibre—here from the left—fell, together with the shadow of that fibre, across the facing ridge of a 45°–90°–45° Au/Cr mirror-coated beam-splitting prism. The prism caused the two photodiode detector elements PDa and PDb to appear to merge, via reflection, along the ridge of the prism. The moving shadow of the fibre therefore slipped seamlessly across the detector from one element to the other. *VM* oscillations on the fibre therefore generated *AC* photocurrent components flowing in anti-phase in PDa and PDb.

5. The scanning system

Figure 4 shows two views of the complete scanning apparatus. This apparatus allowed the vertically-orientated, tensioned, silica test-fibre to be translated at a constant rate so that it passed from side-to-side through the collimated NIR beam linking the shadow-sensor's emitter and detector.

Parenthetically, a very constant (and low) rate of translation of the fibre through the emitter's NIR beam turned out to be essential, in order to avoid apparently variable spatial rates of change of shadow signal—in particular, as the fibre's shadow passed from detector element PDa to element PDb. Such variable rates of change did arise, initially, in this work, before the discovery that they actually were artefacts of the frequency-dependent cross-over network within the Transimpedance Amplifiers block, which was used to separate, conveniently, the *AC* from the *DC* photocurrents. Generally, scanning rates in the range 50–60 μm s^{-1} were used, with a constancy of translation rate at the 0.1 % level. This was achieved by utilizing the atypical constant-speed *DC* motor controller, described below.
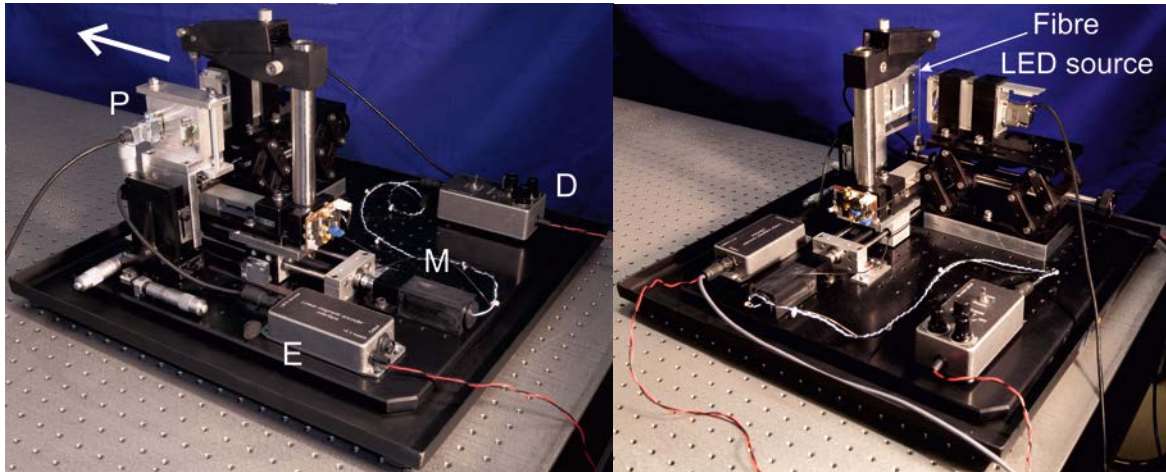
5

Figure 4. Two views of the complete scanning apparatus. Left: rear view of the dual shadow detector housing (P), mounted on a 3-axis micrometer-adjustable stage. Only one of the two synthesized-split-photodiode detectors which were located within this housing was employed, at a time. Here, only the leftmost detector (seen from the rear of the housing) was in use. In the Figure, D houses the *DC* motor driver (Figure 5), M is the in-line motor plus gearbox, and E houses the position encoder interface (Figures 8 and 9). Right: The emitter (LED source) is seen mounted on an adjustable Lab-jack, which was used to set its elevation to coincide with the mid-plane of the silica test-fibre sample (labelled Fibre). The *DC* motor-driven leadscrew translated the test-fibre in its holder slowly (over a period of 4–5 minutes), so that it passed laterally through the NIR beam coming from the emitter to the detector (please see Figure 1). The bold arrow in the Left Figure indicates the scanning sense of the fibre sample. All of the scanner's components were mounted onto the optical baseplate in the photos, this having 45° angled corners. The—essentially—square baseplate measured 440 mm on a side. The 190 mm track of the linear stage had microswitches at its ends, to prevent over-run of the stage's driven carriage.
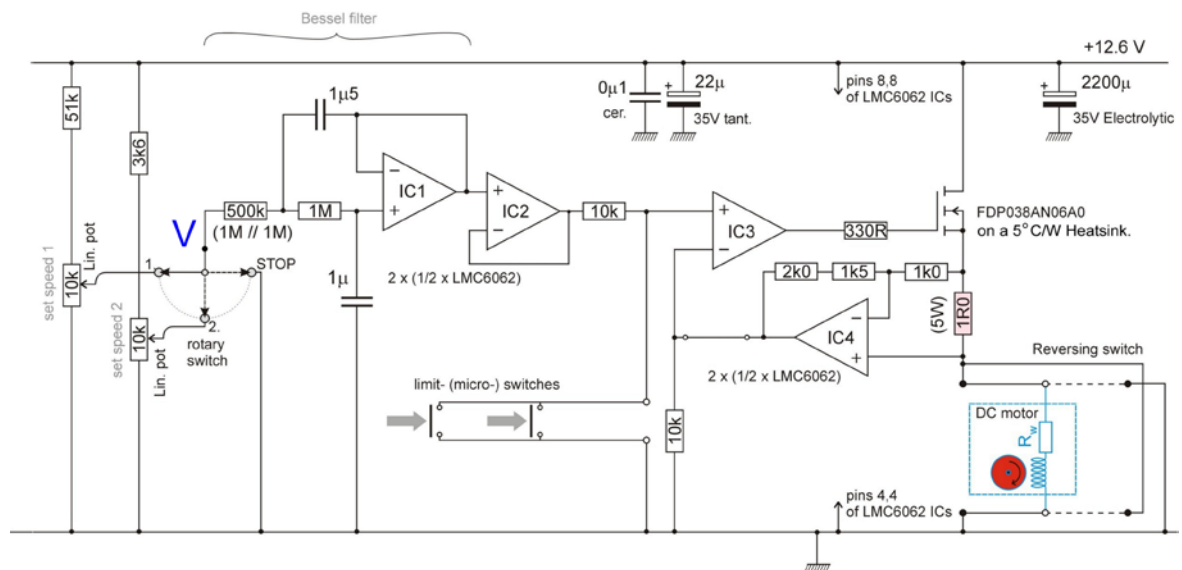

Figure 5. Circuit diagram of the constant-speed *DC* motor driver (D, in Figure 4). The control voltage (point V in the circuit diagram), which governed the motor's speed of rotation, was set using one of two switch-selectable potentiometers: 'speed 1' or 'speed 2' (or STOP). This circuit kept the speed of rotation of the motor constant, in spite of any varying load torque due to the attached gearbox and leadscrew-driven stage. It was achieved by effectively cancelling-out the winding resistance of the *DC* motor, and its leads ($R_w = 3.5 \, \Omega$). Please refer to the text. The motor (a 9 volt *Maxon A*-max 110119) was used to drive an Ondrives LA7-30002 leadscrew-actuator stage via a 1621:1 planetary reduction gearbox (*Maxon* GP 22 A 110341). The circuit's Bessel filter forced any changes of speed to take place smoothly over ~ 5 seconds, with neither over- nor under-shoot. The two microswitches brought the motor to an abrupt halt, should it approach either end of the leadscrew-driven stage's track.

5.1. The constant-speed DC motor controller

The constant motor speed circuit shown in Figure 5 was based upon a scheme which used a current-sensing resistor placed between a 'floating' *DC* motor and ground, and which employed a high-power OPA548 operational amplifier to drive the motor [14].

In this work, however, the *DC* motor and sensing resistor were reversed, thereby connecting the motor usefully to ground on one side, whilst the current-sensing resistor was made to float, as shown in Figure 5. Furthermore, the relatively high value of stall current (2.8 A), which was required at times by the motor, was met by placing a power MOSFET (FDP038AN06A0) within the feedback loop of a low-power op-amp (IC3: ½ × LMC6062).

The circuit functioned as follows: op-amps IC3 and IC4 compensated for the *DC* motor's winding resistance plus connecting leads, labelled R_w (= 3.5 Ω) in the Figure, by creating effectively a cancelling—negative resistance—of this value in series with the motor itself. Through this compensation, the circuitry around these two op-amps forced the motor's back e.m.f. to be equal to the voltage applied to the non-inverting input of IC3—which was itself equal, under steady state conditions, to the input voltage set at the point V in the circuit. Since the motor's back e.m.f. was necessarily directly proportional to its rotational speed, this compensation forced the motor's speed to be held constant, for a constant input voltage—*irrespective of any changes in frictional torque, or load, on the motor.*
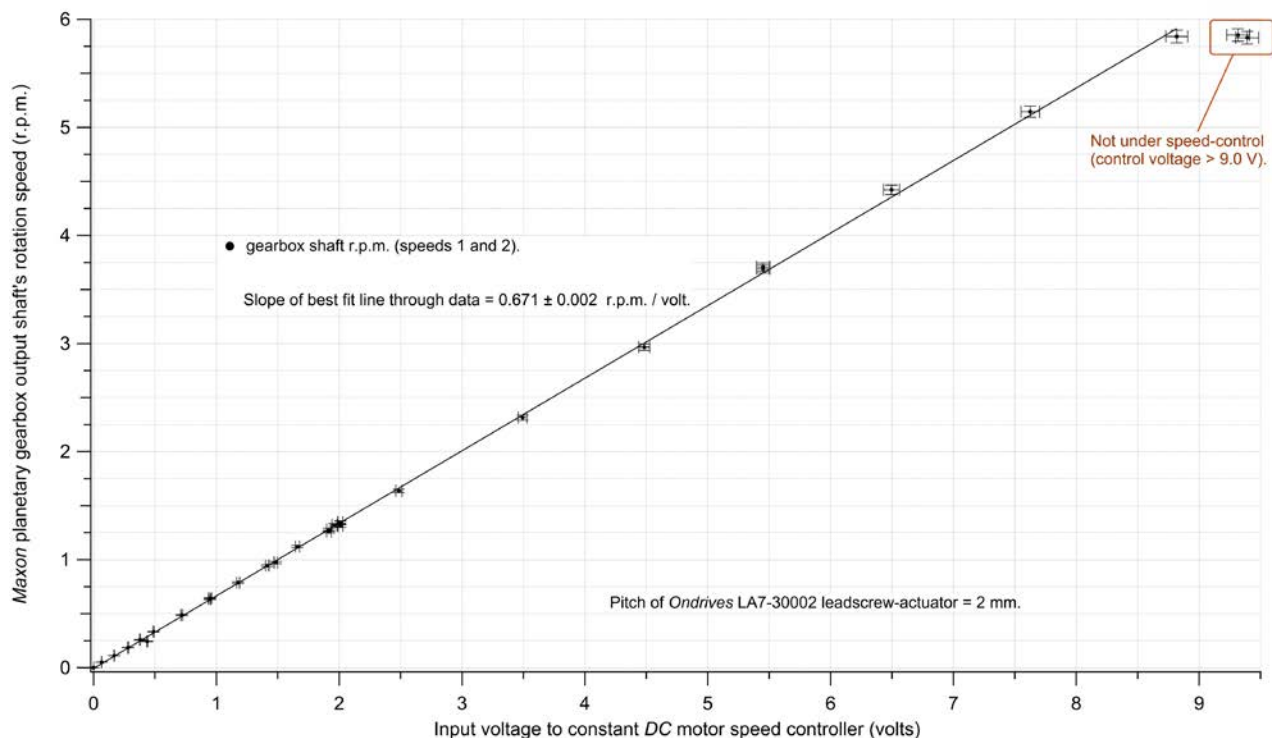

Figure 6. In the Figure the 'r.p.m.' ordinate refers to the output shaft of the 1621:1 planetary reduction gearbox, which drove the leadscrew-actuator. The 'Input voltage' abscissa refers to the voltage used to set the constant speed of the 9 volt *DC* motor, which drove the gearbox. This voltage (at point 'V' in Figure 5) therefore determined the constant traversing rate of the linear stage. Voltage V was set by single-turn potentiometers according to the 'speed 1/speed 2/STOP' setting of the 3-position switch shown in Figure 5. The graph shows, clearly, that the traversing rate was directly proportional to the applied control voltage, as anticipated (for input control voltages < 9 V). As the pitch of the driven leadscrew was 2 mm, this graph shows the maximum rate of traverse for the driven stage to have been ~ 0.2 mm / second. The minimum speed of traverse was < 1 μm / second, as indicated in Figures 7 and 10.

When switching from one set value of the input control voltage V, on the 'speed 1' range (say), to another, on the higher 'speed 2' range (say)—or to STOP (zero volts), abrupt changes in the value of V could occur. The Bessel filter circuitry, built around ICs 1 and 2, caused changes in actual motor speed, due to possibly abrupt changes in the input voltage V, to take place quite smoothly—over a period ~5 seconds in fact, with negligible over- or under-shoot. The limit (micro-) switches shown in Figure 5 pulled the control voltage instantly to zero, however—stopping the motor immediately, and preventing any further travel, if the ends of the linear scanning stage's range were ever approached. In Figure 5, reversal of the stage's sense of translational direction took place at zero command voltage, and so zero translational speed, via the mechanical reversing switch shown in the Figure.

Figure 6 shows the resulting linearity of rotation rate with applied control voltage (for input control voltages V < 9 volts), as a result of using the constant-speed controller shown in Figure 5. Here, the rotation rate was measured at the output shaft of the 1621:1 reduction gearbox.

5.2. Interface for eliminating 'jitter' from the magnetic linear encoder: the 'dither filter'

The *DC* motor driven translation stage was fitted with a *Renishaw* LM10 magnetic linear (incremental) position encoder, the pickup head of the encoder being attached to the moving carriage, and a magnetically-encoded self-adhesive ribbon track being attached to the aluminium alloy optical baseplate. Figure 7 shows the digital quadrature phase output signals A and B from the linear encoder, as the carriage of the translational stage—
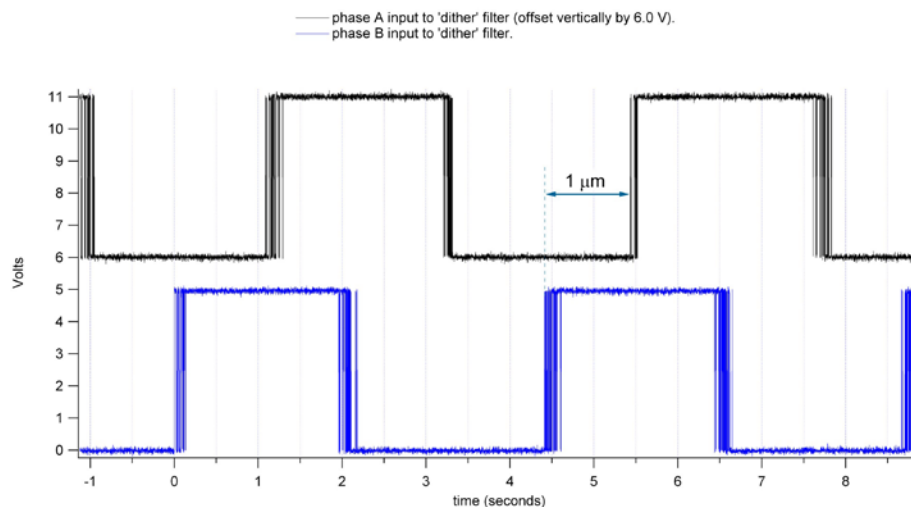

Figure 7. The Renishaw LM10D01_07 linear magnetic encoder, with 1 μm position resolution, was intended for use primarily at higher translation rates (up to 4 m.s^{-1}). It was not optimised for use at very low translation rates, and the Figure shows typical phase A and phase B outputs from this magnetic position sensor at a very low translation rate of ~ 0.9 μm.s^{-1}. The two phase outputs are seen to be correctly in quadrature, but with significant dither-induced noise at their transitional switching edges—possibly induced by the leadscrew drive of the mechanical translation stage. These signals were the inputs to the dither filter of Figures 8 and 9.

carrying the silica test-fibre in its holder—was moving very slowly at a constant rate parallel to this track: here, at a translation rate of ~ 0.9 μm.s^{-1}. Besides the two quadrature phase signals shown in the Figure, the encoder also provided a datum signal (denoted by Z in Figure 8), so that absolute positions of the test-fibre relative to that datum point could be recorded. Figure 7 demonstrates that the switching edges of the digital A and B phase outputs from the magnetic encoder could be corrupted severely by dither noise at the very low translation rates used in this work, and such signals could not be used reliably to keep track of the moving carriage's position. The source of this dither was possibly vibration

coming from the motor/gearbox/leadscrew. Even at the somewhat higher translation rates which were generally used for profiling the shadow-notches, as described in §1.3, and §6, these signals still could be corrupted. Consequently, a bespoke digital interface was designed and implemented, in order to overcome this problem (shown as E in Figure 4).

The two quadrature signals A and B from the encoder were 'cleaned' using a microcontroller based dither-filter, which functioned as a transition noise eliminating interface. Its circuit diagram is shown in Figure 8. This interface also generated brief (1.6 μs) synchronising (CLK) pulses on every edge of the cleaned quadrature signals A_out and B_out, so that these pulses could be used to trigger data capture of the detector's output voltages VDC,a and VDC,b as a function of the silica test fibre's position. In this way, the detector's two DC voltages, VDC, a and VDC, b, were recorded simultaneously at every 1 μm step, and with 12-bit resolution, using a National Instruments USM-6259 DAQ device, controlled by a LabView data acquisition program running on a Laptop PC.

The dither filter shown in Figure 8 functioned as follows: the noisy quadrature phase input signals A and B were threshold detected and 'squared-up' by the CMOS NAND-Schmitt logic gates, before being read into the digital inputs PA0 and PA1 of a PIC16F684 microcontroller (MCU). The MCU used the algorithm shown in Figure 9 to remove the dither (jitter) transitions from these generally low frequency signals, and 'cleaned' versions A_out and B_out of the original signals A and B, respectively, were written out on the MCU's output pins PC0 and PC1. As the rising edge of the zero-datum (Z) output from
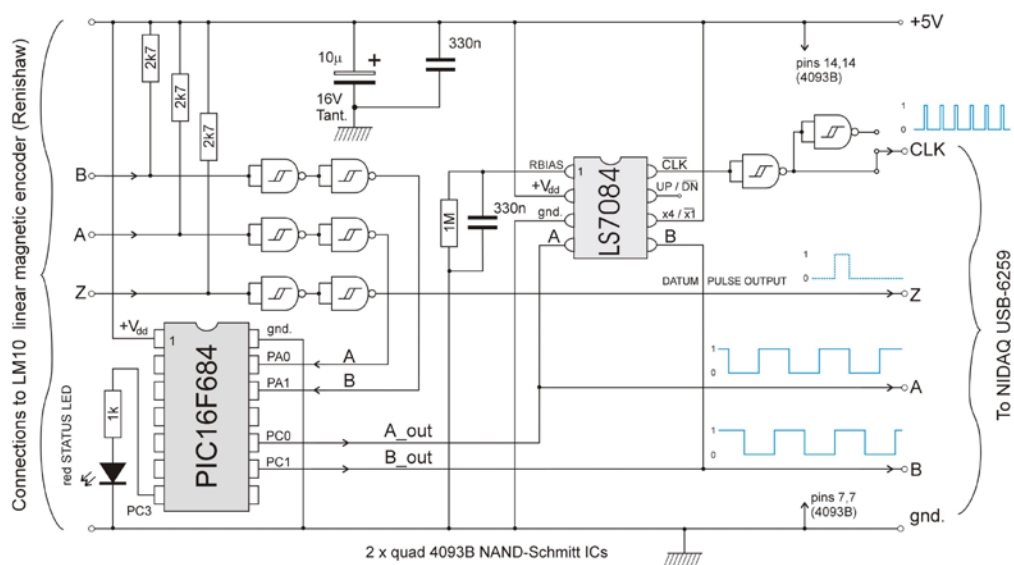

Figure 8. Circuit diagram of the magnetic position encoder's dither filter. The digital input signals to this filter, labelled A, B, and Z, were respectively the two quadrature outputs, and the datum output, from a Renishaw LM10D01_07 linear magnetic encoder. At low translation rates, A and B exhibited significant jitter around their logic transitions, as shown in Figure 7. An LS084 IC generated automatically a clock pulse (CLK) on each 'cleaned' quadrature edge. The CLK (trigger) pulses were 1.6 μs wide: they were used to trigger data capture (please refer to the text). The PIC16F684 MCU ran at an 8 MHz internal clock frequency. An example of the now-cleaned signals is shown in Figure 10.

the encoder always fell correctly between successive edges of signals A and B, it did not require cleaning. The red STATUS LED (normally off) was flashed 3 times only on start-up, when +5 V power was applied to the MCU, to indicate the correct functioning of its operating program. Figure 9 shows the algorithm used by the MCU to remove jitter from the LM10's quadrature phase outputs A and B. The algorithm used a system of flags to determine if phase transitions were allowable, i.e., followed a permissible pattern on the encoder's outputs A and B,

9

or not, ignoring dither transitions (jitter) that formed no proper part of this pattern. The algorithm also used one special case on start-up, where there was no previous history of transitions, and a second special case for circumstances in which the stage had been brought to rest—perhaps preparatory to a change of translational direction. In this latter case a simple timer was used, based on a 50 μs delay and two counters (counter_A and counter_B), these
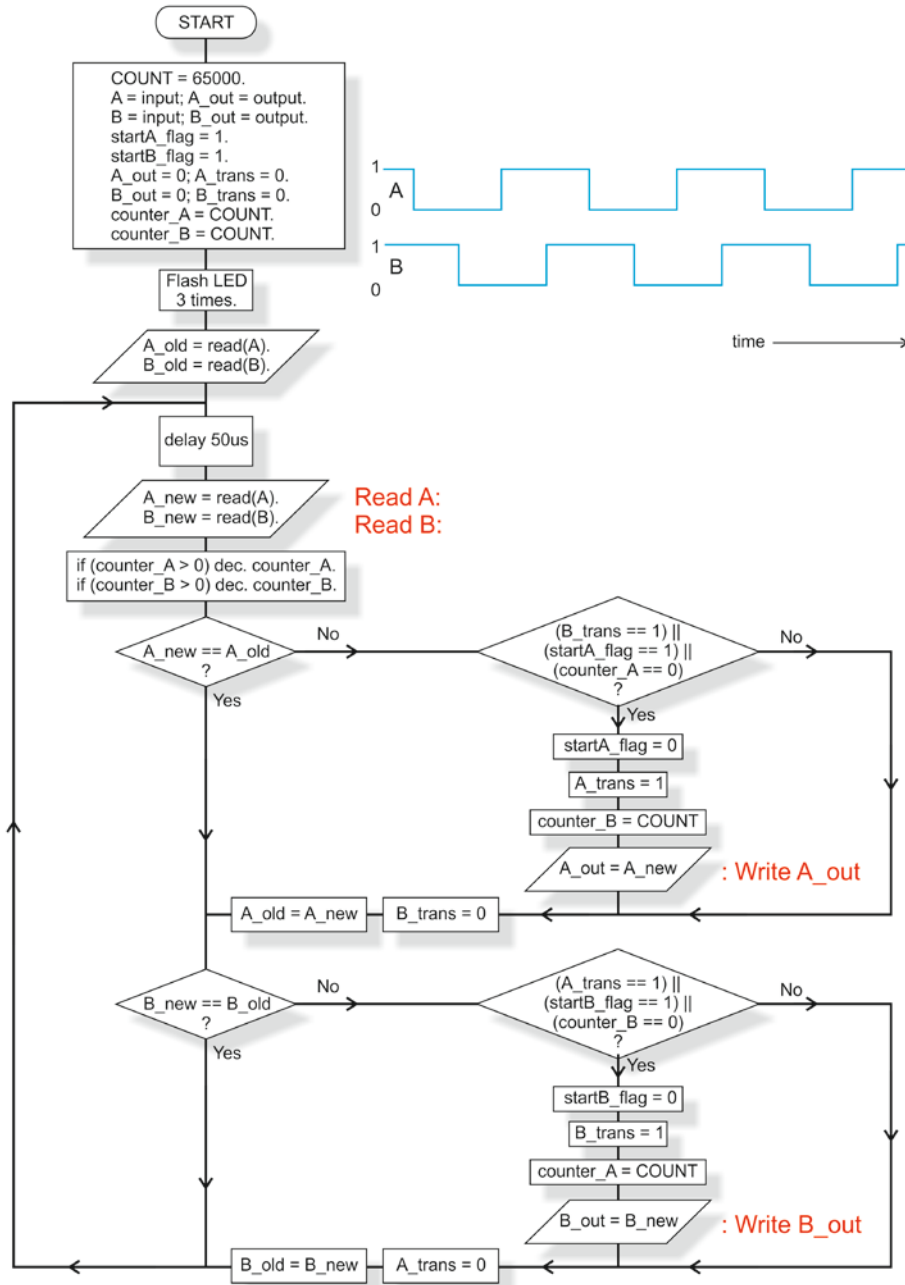

Figure 9. Flow chart for the dither filter algorithm running on the PIC16F684 MCU of the digital interface shown in Figure 4. The MCU polled 'noisy' digital signals A and B (as shown in Figure 3), 'cleaned these up' using this algorithm, and then output digital signals A_out and B_out—with the dither noise eliminated (as shown in Figure 8). Please refer to the text for a description of the algorithm's operation.

being continuously reloaded under normal traversing of the driven stage with a given count value (COUNT = 65000), but whose value decremented to zero, otherwise—taking ~ 3.5 seconds to enter this new mode of operation, where subsequent motion might develop a new pattern of digital transitions.
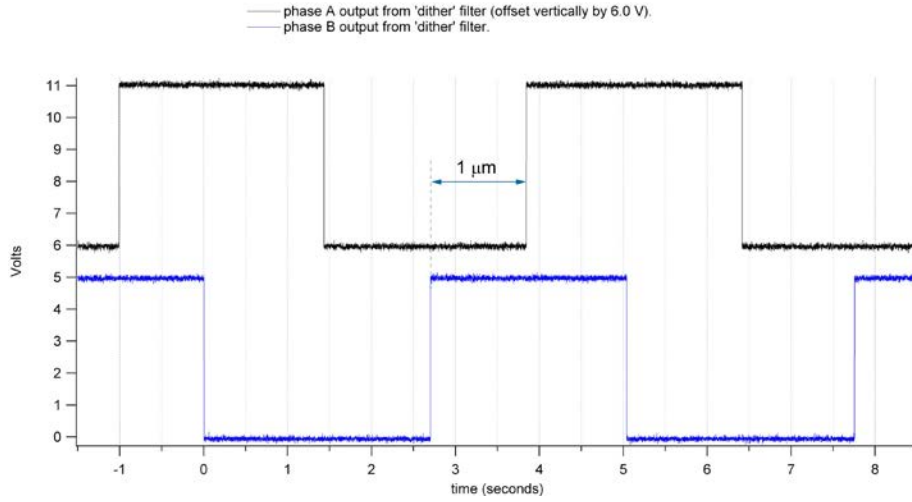
Figure 10. Digital phase signals A_out and B_out from the microcontroller-based 'dither filter' shown in Figures 8 and 9—in this example for a very low translation rate of ~ 0.8 µm.s^{-1}. The filter's two phase outputs are seen to be correctly in quadrature, but with the input dither-induced noise eliminated.

6. Measurement of the *DC* displacement responsivity

Figure 11 shows an example of a pair of detected 'shadow notch' signals, these being generated by the detector's photodiode elements PDa and PDb as the illuminated 400 µm diameter test-fibre sample was translated linearly across in front of them. The fibre's developing position was generated by the National Instruments DAQ device, which was configured to read the Z, A (A_out), and B (B_out) inputs from the dither filter. Simultaneously, the DAQ sampled and stored the *DC* voltages V*DC*,a and V*DC*,b, shown in the Figure, on every CLK pulse. In reality, these '*DC*' responses were convolutions between the fibre's actual shadow and the width of each detector element (0.86 mm, on average).

In point of fact, although the traces in Figure 11 show some curious, and largely symmetrical, features, it was just the cross-over region of approximately ±100 µm, where the fibre's shadow passed from one element to the other—increasing the photocurrent in the first, whilst diminishing that in the second—which was the useful range: this was the region of interest over which Violin-Mode *AC* signals were to be detected, as indicated in the Figure.

Indeed, the '*DC* displacement responsivity to quasi-static displacement' was found from the rate of change with respect to fibre position ξ of the difference between the two signals V*DC*, a and V*DC*, b shown in the Figure. In this example, the *DC* displacement responsivity was measured to be 10.0 kV. m^{-1} at the ξ = ±0.1 mm end-of-span points—peaking at 13.5 kV.m^{-1} (at ξ = 0). The *AC/DC* responsivity ratio was 904 ± 4 at 500 Hz (rather than 1000, as mentioned in §4), due here to the roll-off of the amplifier's pass-band towards low frequencies. Therefore, the *AC* (Violin-Mode) displacement responsivity to vibrational displacement at the *VM* frequency of 500 Hz was found, straightforwardly, from this calibration to be 9.04 MV (rms) m^{-1} (rms), at the end-of-span positions, for this particular sensor.

The end-of-span responsivity values were used to characterize the shadow sensors, and, over the four sensors of the full shadow-sensing system, the calibration system described here found the *AC* (Violin-Mode) displacement responsivity to vibrational displacement to be (9.45 ± 1.20) MV (rms) / m (rms), at 500 Hz. Taken together with the measured noise level at the amplifier's *VM AC* output (on average, equal to [−64.0 ± 0.5] dBV (rms) / √Hz), this led to a

VM displacement sensitivity of (69 ± 13) picometres (rms) / $\sqrt{\text{Hz}}$, at 500 Hz, when taken across the four shadow-sensors [8,9].
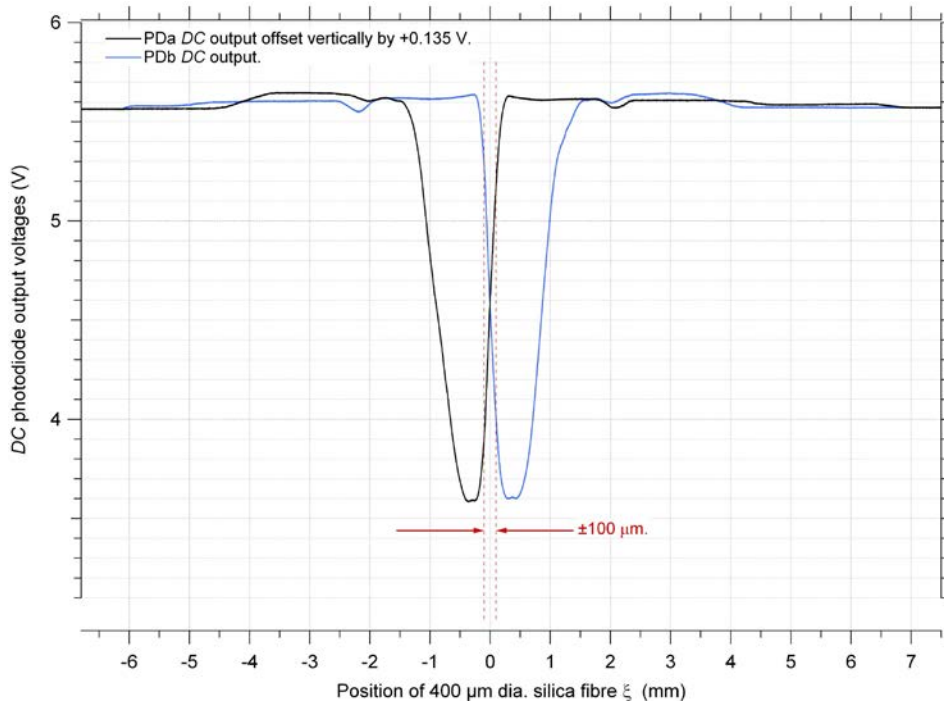

Figure 11. Shadow-notch signals V*DC*, a and V*DC*, b from adjacent photodiode elements PDa and PDb, respectively. These data were captured with 12-bit resolution at every 1 μm change in position of the silica test-fibre sample, using the CLK signal (shown in Figure 8) as the sampling trigger. Here, the silica test-fibre was scanned slowly in the positive ξ-direction, so that its shadow fell first onto photodiode element PDa, and then onto element, PDb.

7. Conclusions

An off-the-shelf solution could not to be justified for this one-off application. Moreover, there were significant advantages in choosing this bespoke approach. Ongoing experimentation with the shadow-sensors informed the need for very low, and constant speed, translation rates, in order to achieve good repeatability in measurements of the *DC* (and hence, *AC*) responsivities, or 'slope-sensitivities,' of the shadow-sensors. Indeed, this iterative process determined the useful range of translational rates to lie between ~200 μm s^{-1} to below 1 μm s^{-1}, allowing a constant-speed motor controller to be designed and built which bracketed just this useful range, via a 0–9 volt control voltage. Also, manual control of the scanning process was found to be sufficient for this (not particularly repetitive) task, and control of it via a PC was felt to be unnecessary—although the data captured by the DAQ were of course displayed in real time on a PC, appearing as in Figure 11.

The equipment proved to be reliable, and, most importantly, this calibration system gave reproducible results for all of the shadow-sensors that were tested. Indeed, they guided the design of these sensors, so that, overall, all four sensors turned out to have similar displacement responsivies, at (9.43 ± 1.20) MV (rms) / m (rms), at 500 Hz. These *DC* responsivity calibrations, together with the corresponding noise measurements detailed in [9,13], led to an average displacement sensitivity, taken over all four shadow-sensors of the *VM* detection system, of (69 ± 13) picometres (rms) / $\sqrt{\text{Hz}}$, at 500 Hz, over a span of ±0.1mm—which exceeded their design target.

8. Acknowledgements

References

[1]   Abbott B P *et al*   2009 LIGO: The Laser Interferometer Gravitational-Wave Observatory *Rep. Prog. Phys.* **72** 1–25.

[2]   Raab F J *et al*   2004 Overview of LIGO Instrumentation *Proceedings of SPIE* **5500** 11–24 (29 Sept.).

[3]   Aston S M et al 2012 Update on quadruple suspension design for Advanced LIGO Class. Quantum Grav. 29 235004 (25pp).

[4]   Heptonstall A *et al*   2011 Invited Article: CO_2 laser production of fused silica fibres for use in interferometric gravitational wave detector mirror suspensions *Rev. Sci. Instrum.* **82**, 011301 1–9.

[5]   Cumming A V *et al* 2012 Design and development of the advanced LIGO monolithic fused silica suspension *Class. Quantum Grav.* **29** 035003 (18pp).

[6]   Carbone, L., et al. 2012 Sensors and actuators for the Advanced LIGO mirror suspensions. *Classical and Quantum Gravity* 29 11 115005 (14pp).

[7]   Dmitriev A *et al* 2010 Controlled damping of high-Q violin modes in fused silica suspension fibres. *Class. Quantum Grav.* **27** 025009 (8pp).

[8]   Lockerbie N A and Tokmakov K V   TBA   A 'Violin-Mode' shadow sensor for interferometric gravitational wave detectors. *Document No. P1100046-v2 available at https://dcc.ligo.org/. (*TBA *Class. MST.).*

[9]   Lockerbie N A, Tokmakov K V, and Strain K A   A source of illumination for low-noise 'Violin Mode' shadow sensors, intended for use in interferometric gravitational wave detectors. *Document No. P1100047-v2 available at https://dcc.ligo.org/. (*TBA *MST.).*

[10] González G. I. and Saulson P. R. 1994 Brownian motion of a mass suspended by an anelastic wire J. Acoust. Soc. Am. 96, 207 (6pp).

[11] Braginsky V.B., Mitrofanov V.P., and Tokmakov K.V. 1996   Energy dissipation in the pendulum mode of the test mass suspension of a gravitational wave antenna *Physics Letters A* 218 3–6 (3pp).

[12] Lockerbie N A et al 2011 First results from the 'Violin-Mode' tests on an advanced LIGO suspension, at MIT. *Class. Quantum Grav.* 28 245001 (12pp).

[13] Lockerbie N A and Tokmakov K V, 2014 A low-noise transimpedance amplifier for the detection of 'Violin-Mode' resonances in advanced LIGO suspensions. *LIGO Document P1400103-v1 available at https://dcc.ligo.org/*.

[14] Trump B 1999 DC MOTOR SPEED CONTROLLER: Control a DC Motor without Tachometer Feedback Burr-Brown application note AB-152 (2pp).